Dual-Input Quasi Z-Source PV Inverter

Dynamic Modeling, Design, and Control

Lashab, Abderezak; Séra, Dezso; Rodrigues Martins, João Pedro; Guerrero, Josep M.

Published in:
I E E E Transactions on Industrial Electronics

DOI (link to publication from Publisher):
10.1109/TIE.2019.2935927

Publication date:
2020

Document Version
Accepted author manuscript, peer reviewed version

Dual-Input Quasi Z-Source PV Inverter: Dynamic Modeling, Design, and Control

Abderezak Lashab, *Student Member, IEEE,* Dezso Sera, *Senior Member, IEEE,* Joao Martins, *Student Member, IEEE,* and Josep M. Guerrero, *Fellow, IEEE*

***Abstract*—In the conventional photovoltaic (PV) fed quasi-Z (qZ) network-based impedance-source-converters (ISCs), the PV array is connected to their input, whereas in the proposed topology in this paper, an additional array is paralleled to the second qZ-network's capacitor (*C*). This modification allows harvesting more PV power through full utilization of the employed qZ-network in the classical ISCs. Moreover, the proposal offers higher conversion efficiency since the current in the second qZ-network's inductor (i_{L2}) is smaller. The voltage of the added PV array (PV_2) is independent of the voltage of the primary array (PV_1) in a wide range, which promotes tracking their maximum power points (MPPs) separatly, achieving a higher efficiency even under partial shading. The use of two separate MPPTs in one converter is a challenge since the perturbation done by the first MPPT alters the power in PV_2 as well, and vice-versa. Therefore, a two MPPs tracker (MPPsT) algorithm, which perturbs two parameters and observes four variables, is proposed for the presented converter. The theoretical analysis is validated through real-time hardware-in-the-loop tests, and it demonstrates that at least 11% more power can be harvested compared to the conventional qZ-network-based ISC.**

***Index Terms*—Efficiency, Photovoltaic power systems, MPPT.**

I. Introduction

PHOTOVOLTAIC panels produce power with low voltage, which requires boosting the voltage in grid-connected application [1]. Since the conventional voltage source converter (VSC) does not offer the possibility to boost the output voltage, usually, two independent systems, such as two-stage grid-tied system with dc side MPP tracking being the first stage and an inverter side doing grid power injection control, are used [2]-[3]. This double-staged system configuration affects the efficiency negatively as well as the dynamic response of the system corresponding to both changes in grid perturbations and environmental conditions [4]. Another alternative is installing a step-up transformer at the output of the inverter to boost the ac voltage [4], [5]. However, this solution is expensive, lossy, and it may cause high current stress at the transformer's primary side, as well as at the semiconductor switches of the inverter as a result of the high current rating provided by the PV array [5].

The authors are with the Department of Energy Technology, Aalborg University, 9220 Aalborg, Denmark (e-mail: abl@et.aau.dk; des@et.aau.dk; jrm@et.aau.dk ;joz@et.aau.dk).

In 2003, an inverter that is able to perform the above-mentioned power conversion functionalities in one stage called as Z-source inverter (ZSI), has been introduced [6]. This converter consists of a VSC with two inductors, two capacitors, and a diode at its input, which allow two semiconductor switches from the same leg to be gated ON simultaneously [7]-[9]. The latter state is referred to as shoot-through (SH) state in the ZSI's literature [10]-[11].

The qZSI belongs to the family of ZSIs, which has been designed particularly for PV applications since it does not require an input capacitor due to its continuous input current [12]. Moreover, the qZSI uses capacitors with less size, as well as less voltage at the terminal of C_2 [13]. Although the qZSI has been introduced as grid-connected three-phase two-level inverter, its advantageous features made it used in several applications, and investigated by a broad research community [14]-[25]. It has been used in stand-alone in [14], where the authors developed an adaptive neuro-fuzzy inference system-based MPPT for increasing its dynamic performance, thus improving its efficiency. As a dc-dc converter, the qZS has been first proposed in [15], where dc-dc distributed power generation is its applicability, the qZS is connected to a step-up transformer, which is feeding a voltage doubler rectifier. This topology has been extended to a multiphase one for wide input voltage or current in [16]. The qZS has been also used in dc-dc conversion in [17], where multiple submodules were cascaded in order to reach the desired dc-grid voltage. The submodules were fed by PV modules through front-end isolation H-bridge where the aim of interfacing this later is to decrease the control complexity. A battery is feeding an induction motor of electric vehicle through a bidirectional dc-ac qZSI in [18], where the qZ-network's diode is replaced by an active switch for backing up the energy to the battery. This topology has been used again in [19], but by moving the battery to be in parallel to C_2 and installing an ultracapacitor at the input of the converter. In order to optimize the dynamic power regulation in the qZ-network, thus increasing the life span of the battery in this topology, the authors developed a frequency dividing coordinated control approach for it. The qZSI has been proposed as a multilevel dc-ac converter in [20], where a detailed modeling and design guidelines of the converter have been presented. For this topology, a control strategy based on distributed MPPT and space vector modulation to ensure the staircase voltage waveform in the presence of the SH states has been developed in [21]. A matrix converter based on qZ-network has been introduced in [22], where it has been applied to a four-quadrant controlled induction motor, ensuring that

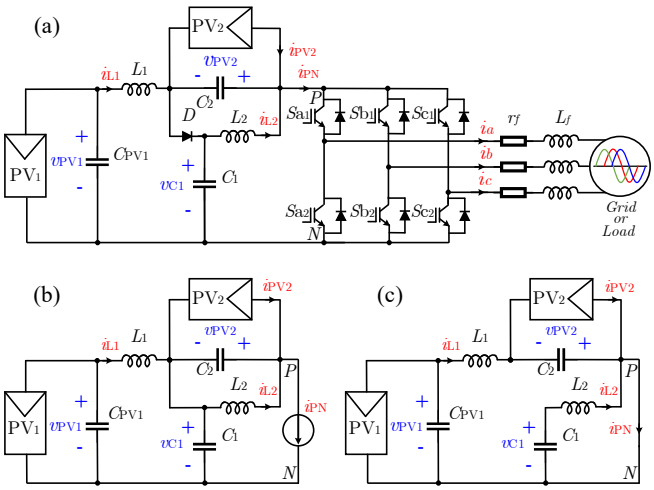

Fig. 1. (a) The proposed DI-qZSI for PV systems, and its equivalent circuit during; (b) active states; and (c) shoot-through state.

the burden of voltage gain limitation is coped with. In order to mitigate the power fluctuations resulted from the changing weather conditions, two level and multilevel qZSIs with integrated energy storage have been proposed in [23] and [24], respectively. Although impedance design methods for the PV fed qZSI with energy storage are presented in [25], a comparative investigation on the converter with and without the added energy source is still missing in the literature.

When several PV modules are connected in series/parallel, and during partial shading, several MPPs appear on the $P(v)$ curve, and the one corresponding to the highest power is usually referred to as the global MPP (GMPP). Clearly, in order to extract the highest power possible, the PV modules sum should operate at GMPP; however, the classical MPPTs such as, Perturb & Observe and Incremental Conductance, among others, usually fail into reaching that point as they get trapped in the first MPP point they encounter. To cope with this issue, metaheuristic-based MPPTs such as genetic algorithm, particle swarm optimization, artificial bee colony, grey wolf have been developed [26]. Nevertheless, operating the PV array at GMPP makes every PV module operate away from its local MPP, leading to a degraded efficiency. In the literature, there are several PV configurations, where the PV modules can be distributed, such as module integrated configuration, and cascaded multilevel configuration. Although these configurations reach higher efficiency, they are costly as a micro-inverter is installed for each PV panel.

In this paper, a dual-input (DI) qZSI is proposed, where an extra PV array is installed in parallel to C_2, allowing more power harvesting through full utilization of the employed qZ-network in the classical qZSI. Moreover, the MPPs of the two arrays can be tracked separately, which ensures an optimized system efficiency even during partial shading. The employment of two separate MPPTs in one converter is a challenge since they affect one another; therefore, an MPPsT algorithm, which perturbs two parameters, namely the SH duty cycle (D_{sh}) and the modulation index (M), and observes four variables, is proposed for the presented topology.

II. DI-qZSI Topology

If a PV array is connected in parallel to C_2, the configuration of the qZSI is as shown in Fig. 1(a). To investigate the DI-qZSI, the equivalent circuits of the converter during both SH and non-SH are given in Fig. 1(b) and (c), respectively. During the SH state, at least one of the bridge's legs is short-circuited, making the current increase in the qZ-network at the expense of the energy stored in the capacitors, which moves the PV arrays' operating points toward their short circuit currents (i_{SC}). According to Fig. 1(c), the energy stored in C_{PV1} is released in L_1, whereas C_1 discharges into L_2. After the SH ends, when the active state starts, the capacitors charge again until the inductor currents decrease. As sketched in Fig. 1(b), PV_1 and L_1 boost C_1 voltage, whereas PV_2 and L_2 boost C_2 voltage. At the meanwhile, the PV arrays inject also power to the grid/load.

III. Dynamic Modelling of the DI-qZSI

For simplification, it is assumed that the diode D on-resistance r_{ON} is negligible in the mathematical derivation since the load impedance is much higher than r_{ON}. The voltage drop in D and the qZSI capacitors stray resistances are also omitted. In case PV_2 is under high solar irradiance while PV_1 is shaded, the diode D may block during some time of the active state since the larger amount of the current would pass by PV_2 instead of D. The later case is disregarded in the mathematical derivation.

Considering L_1 and L_2 currents, C_1 and PV_2 voltages as the state space variables $\boldsymbol{x}=[i_{L1},\ i_{L2},\ v_{C1},\ v_{PV2}]^t$, the state space model during non-SH state can be given as,

$$\mathbf{F}\cdot\frac{d\boldsymbol{x}}{dt}=\mathbf{A}_1\cdot\boldsymbol{x}+\mathbf{B}_1\cdot\boldsymbol{u} \tag{1}$$

such as,

$$\mathbf{A}_1=\begin{bmatrix}-r_{L1} & 0 & -1 & 0\\ 0 & -r_{L2} & 0 & -1\\ 1 & 0 & 0 & 0\\ 0 & 1 & 0 & 0\end{bmatrix};\ \mathbf{B}_1=\begin{bmatrix}1 & 0 & 0\\ 0 & 0 & 0\\ 0 & 0 & -1\\ 0 & 1 & -1\end{bmatrix},$$

$$\boldsymbol{u}=\begin{bmatrix}v_{PV1}\\ i_{PV2}\\ i_{PN}\end{bmatrix},\ \text{and}\ \mathbf{F}=\text{diag}(L_1\ L_2\ C_1\ C_2)^t$$

where r_{L1} and r_{L2} are the stray resistances of the inductors L_1 and L_2, respectively, v_{PV1} is PV_1's voltage, i_{PV2} is PV_2's current, and i_{PN} is three-phase inverter bridge's input current.

During the SH states, the model can be obtained as,

$$\mathbf{F}\cdot\frac{d\boldsymbol{x}}{dt}=\mathbf{A}_0\cdot\boldsymbol{x}+\mathbf{B}_0\cdot\boldsymbol{u} \tag{2}$$

such as,

$$\mathbf{A}_0=\begin{bmatrix}-r_{L1} & 0 & 0 & 1\\ 0 & -r_{L2} & 1 & 0\\ 0 & -1 & 0 & 0\\ -1 & 0 & 0 & 0\end{bmatrix};\ \mathbf{B}_0=\begin{bmatrix}1 & 0 & 0\\ 0 & 0 & 0\\ 0 & 0 & 0\\ 0 & 1 & 0\end{bmatrix},$$

By using the average state approach, the average state space model can be obtained as (3) below,

$$\mathbf{F}\cdot\frac{d\boldsymbol{x}}{dt}=\mathbf{A}\cdot\boldsymbol{x}+\mathbf{B}\cdot\boldsymbol{u} \tag{3}$$

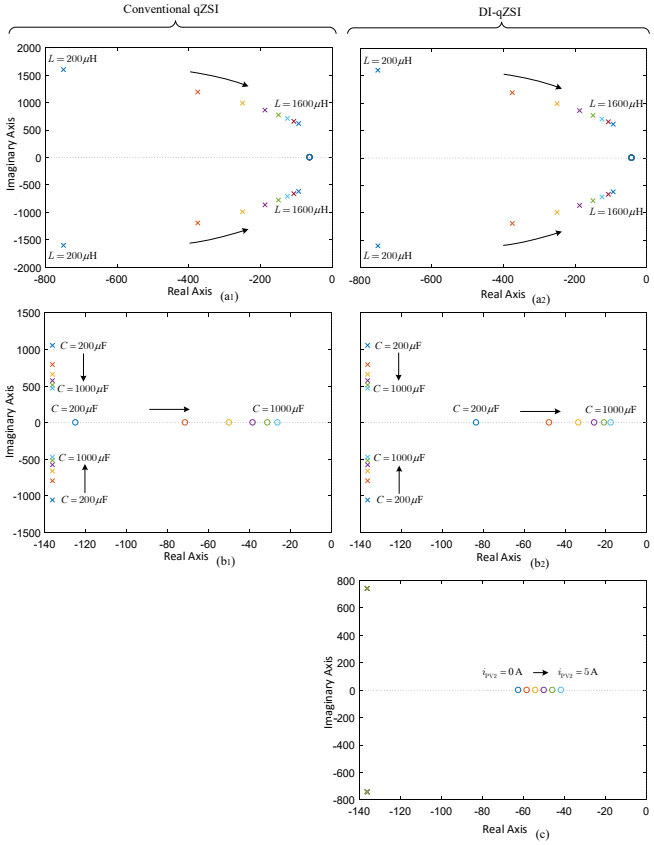

Fig. 2. Root loci of $\tilde{d}_{sh}$ to $\tilde{i}_{L1}$ transfer function: (a_1) inductor L and (b_1) capacitor C sweeps in the traditional qZSI; and (a_2) inductor L, (b_2) capacitor C and (c) i_{PV2} sweeps in the DI-qZSI.

where,

$$\mathbf{A}=\begin{bmatrix} -r_{L1} & 0 & D_{sh}-1 & D_{sh} \\ 0 & -r_{L2} & D_{sh} & D_{sh}-1 \\ 1-D_{sh} & -D_{sh} & 0 & 0 \\ -D_{sh} & 1-D_{sh} & 0 & 0 \end{bmatrix};\ \mathbf{B}=\begin{bmatrix} 1 & 0 & 0 \\ 0 & 0 & 0 \\ 0 & 0 & D_{sh}-1 \\ 0 & 1 & D_{sh}-1 \end{bmatrix},$$

The small signal model of the proposed DI-qZSI can be obtained by applying Laplace on (1) and (2), along with introducing a perturbation on each of the output signals v_{PV1}, i_{PV2}, and i_{PN}, separately. Each of the output signals is going to be substituted by $u=U+\tilde{u}$ (where U is the equilibrium point and $\tilde{u}$ is the introduced perturbation of the output variable). These perturbation induce back perturbations on the state space variables $x=X+\tilde{x}$ (where X is the equilibrium point and $\tilde{x}$ is the induced perturbation in the state space variable).

The transfer function from $\tilde{d}_{sh}$ to $\tilde{i}_{L1}$ is used for investigating the system stability and parameters design, and it can be assessed from the derived small signal model as follows,

$$G_{\tilde{d}_{sh}}^{\tilde{i}_{L1}}(s)=\left.\frac{\tilde{i}_{L1}}{\tilde{d}_{sh}}\right|_{\substack{\tilde{i}_{PN}=0\\ \tilde{i}_{PV2}=0\\ \tilde{v}_{PV1}=0}} = \frac{(V_{C1}+V_{C2})Cs+(I_{L1}+I_{L2}-I_{PN})(1-2D_{sh})}{LCs^2+Cr_Ls+(1-2D_{sh})^2} \quad (4)$$

In (4), it is assumed that $C=C_1=C_2$ and $L=L_1=L_2$. The transfer function from $\tilde{i}_{L1}$ to $\tilde{v}_{PV1}$, $G_{\tilde{i}_{L1}}^{\tilde{v}_{PV1}}(s)$ can be derived by converting the formula obtained by Kirchhoff's law applied to the input of the DI-qZSI into Laplace domain,

$$G_{\tilde{i}_{L1}}^{\tilde{v}_{PV1}}(s)=\left.\frac{\tilde{v}_{PV1}}{\tilde{i}_{PV1}-\tilde{i}_{L1}}\right|_{\substack{\tilde{i}_{PN}=0\\ \tilde{i}_{PV2}=0\\ \tilde{d}=0}} = \frac{1}{C_{PV1}s} \quad (5)$$

Accordingly, the block diagram of the DI-qZSI model in Laplace domain can be obtained as shown in Fig. 3. One can note that, the transfer function $G_{\tilde{d}_{sh}}^{\tilde{i}_{L1}}(s)$ is similar to that of the classical qZSI [9], except that I_{L1} is not equal to I_{L2} here. The relationship between these two currents can be assessed from (3), considering the corresponding left term approximated to zero during the steady state,

$$i_{PV2}=i_{L1}-i_{L2} \quad (6)$$

The dynamic characteristics of the DI-qZSI are studied by performing various root loci of the transfer function $G_{\tilde{d}_{sh}}^{\tilde{i}_{L1}}(s)$, where the sweep does not only consider the parameters L and C, but also i_{PV2}. The system is identified as: v_{PV1}=300V, i_{PV2}=5A, i_{PN}=15A, D_{sh}=0.25, $C_{1,2}$=400μF, $L_{1,2}$=1mH, and r_L=0.3Ω. For the sake of comparison, the root loci of the traditional qZSI are shown in Fig. 2(a_1), and (b_1), while those of the DI-qZSI are presented in Fig. 2(a_2), (b_2) and (c).

It can be seen from these plots that, employing a loop for i_{L1} increases the system's stability as the zeros are on the left half plane (LHP), which is opposed to using $v_{C1,2}$, such as in [9]. In the latter case, the zeros appear on the right half plane (RHP), which denotes to a nonminimum-phase undershoot, imposing a considerable low-bandwidth in order to acquire a stable system.

One can see from Fig. 2 that, in both the conventional qZSI and the DI-qZSI one, the poles real parts are identical, which indicates that both systems are equivalently stable. It can be observed from Fig. 2(a_1) and (a_2) that, the zeros are pushed from the LHP toward the origin along the real axis in the DI-qZSI. This later shows comparatively higher overshoot for the same qZ-network inductors size, as it is the same case with qZ-network capacitors from Fig. 2(b_1) and (b_2). This overshoot is due mainly to the extra current (i_{PV2}), where it decreases back with respect to i_{PV2} decrease as indicated by Fig. 2(c).

IV. DI-qZSI Topology Design

A. qZS-network passive elements design

The qZ-network inductors are employed to limit the current increase during the SH state. Hence, using the SH model (2), one can get [12],

$$L_2 \simeq L_1=\frac{dt}{di_{L1}}v_{C1} \simeq \frac{\Delta t}{\Delta i_{L1}}\left(v_{PV1}+v_{PV2}\right) \quad (7)$$

such as, Δi_{L1} stands for the desired current ripple, and Δt is the maximum SH duration, which is in case of Simple-Boost PWM (SBPWM) approximated by (8),

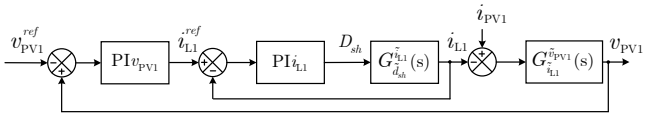

Fig. 3. Block diagram of the PV DI-qZSI model in the Laplace domain.

$$\Delta t = \frac{D_{sh}^{max}}{2 f_s} \tag{8}$$

where f_s is the switching frequency. The capacitor C_1 absorbs the current going through the diode D during the active state, which is according to Fig. 1(b) and Kirchhoff's current law estimated as,

$$C_1 \frac{d\left(v_{\mathrm{PV1}} + v_{\mathrm{PV2}}\right)}{dt} = i_{\mathrm{L1}} - C_2 \frac{dv_{\mathrm{PV2}}}{dt} \tag{9}$$

The capacitor C_2 is best chosen equal to C_1, otherwise, a resonance in the qZ-network may take place [24]. On the other hand, the capacitors C_1 and C_2 absorb both the high-frequency ripple caused by the switching of the semiconductor devices, and also the low-frequency ripple ($6\omega_g$) induced by the oscillatory instantaneous power delivery. Consequently, from (9) the capacitors can be designed as,

$$C_1 \simeq C_2 = \frac{1}{6 f_g \left(\Delta v_{\mathrm{PV1}} + 2\Delta v_{\mathrm{PV2}}\right)} i_{\mathrm{L1}} \tag{10}$$

such as, Δv_{PV1}, Δv_{PV2}, and f_g are, respectively, the desired voltage ripple in $\mathrm{PV_1}$, the desired voltage ripple in $\mathrm{PV_2}$, and the line frequency. As it can be seen from (7) and (10), the qZ-network passives are solely dependent upon $\mathrm{PV_1}$ parameters, while v_{PV2} is considered to have the same voltage level in the absence of $\mathrm{PV_2}$ due to the qZSI boosting function.

B. PV_2 design

By neglecting the stray resistances, and by equating the left term of the average state space equation (3) to zero considering a steady state operating conditions, it can be deduced that,

$$v_{\mathrm{PV2}} = v_{\mathrm{PV1}} \frac{D_{\mathrm{sh}}}{1 - 2D_{\mathrm{sh}}} \tag{11}$$

The voltage of $\mathrm{PV_2}$ with respect to $\mathrm{PV_1}$ is displayed in Fig. 4 according to (11). As it can be observed from both this figure and (7), a high voltage PV panel can be added; however, the design of the qZ-network is strongly dependent upon both the voltage level and the SH duration, as indicated by (7) and (10). Hence, in what follows, it is assumed that the design of the system is based on a maximum SH duty cycle $D_{sh}^{max} = 0.3$.

The relation between the two PV array currents can be extracted from (3) as follows,

$$i_{\mathrm{PV1}} \simeq i_{\mathrm{L1}} = \frac{\left(1 - D_{sh}\right) i_{\mathrm{PN}} - D_{sh}\, i_{\mathrm{PV2}}}{1 - 2D_{sh}} \tag{12}$$

From (12), and by considering that the SH duty cycle is greater than or equal to zero, one can get (13),

$$i_{\mathrm{PV1}} \geq i_{\mathrm{PV2}} \tag{13}$$

This later, shows that for optimal usage of the added PV array, the corresponding nominal current ought to be carefully selected since it should be always less than i_{PV1}. Hence, the size of $\mathrm{PV_2}$ must be selected by considering the lowest levels of i_{PV1} while i_{PV2} is at its nominal level. Accordingly, $\mathrm{PV_2}$ can have:

1) The same nominal current as $\mathrm{PV_1}$, in case the system is installed in an area where the partial shading is extremely rare, such as desertic areas. In this case, $\mathrm{PV_2}$ can have its highest rating, where its power could reach 33% of $\mathrm{PV_1}$ (considering $D_{sh}^{max} = 0.3$).
2) The same nominal current as $\mathrm{PV_1}$, but a moving partial shading is always present e.g. caused by a chimney in case of rooftop installation, or in "nicely" designed installations using modern flexible PV modules. The shadowed panels can be moved to be in parallel to C_2 with their own MPPT, thereby minimizing the yield loss due to shadows at minimum additional cost.
3) A lower nominal current (by installing fewer parallel PV panels in $\mathrm{PV_2}$ compared to $\mathrm{PV_1}$) according to the expected partial shading on $\mathrm{PV_1}$ e.g. installations in nordic countries.

TABLE I.
COMPARISON BETWEEN THE CONVENTIONAL AND THE DI-QZSI

Current stress	Conventional qZSI	DI-qZSI
Active switches	$i_{\mathrm{PV1}}+0.5\Delta i_{\mathrm{L1}}+I_{1\phi}$	$i_{\mathrm{PV1}}-i_{\mathrm{PV2}}+0.5\Delta i_{\mathrm{L1}}+I_{2\phi}$
Diode	$2i_{\mathrm{PV1}}+\Delta i_{\mathrm{L1}}+I_{1\phi}$	$2i_{\mathrm{PV1}}-i_{\mathrm{PV2}}+\Delta i_{\mathrm{L1}}+I_{2\phi}$
$L_{1,2}$	Eq. (7)	Eq. (7)
$C_{1,2}$	Eq. (10)	Eq. (10)
Power harvesting	P_{PV1}	$P_{\mathrm{PV1}}+P_{\mathrm{PV2}}$

C. Semiconductor ratings

According to the analysis presented above both the DI-qZSI and the conventional one share the same qZ-network passives count and size. Regarding the power switches, they still share the same count and voltage ratings; however, on the current aspect, some differences prevail. TABLE I. summarizes a sizing; thus, a cost comparison between the DI-qZSI and the classical one. As it can be seen from this table, although the phase peak-current ($I_{k\phi,\ k=1,2}$) in the DI-qZSI is higher, the current stresses in both the diode and active switches are less than the ones in conventional qZSI since the current conducted by L_2 is less than i_{PV1}, where a part of the later passes through $\mathrm{PV_2}$. Nevertheless, the active switches and diode in the DI-qZSI should be designed for the worst-case scenario, which is during partial shading in $\mathrm{PV_2}$, yielding into similar requirements as in the classical qZSI.

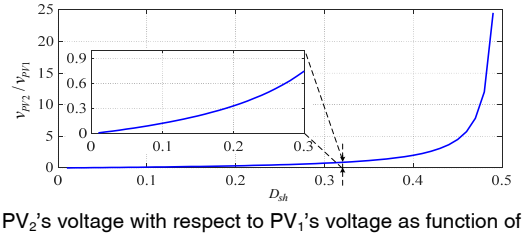

Fig. 4. $\mathrm{PV_2}$'s voltage with respect to $\mathrm{PV_1}$'s voltage as function of D_{sh}.

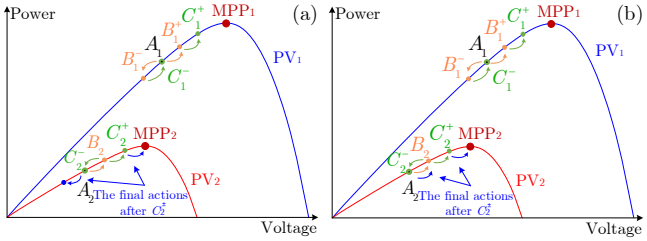

Fig. 5. Operating point movement in case of using; (a) two separate MPPTs; and (b) the proposed MPPsT.

V. Proposed MPPsT for the DI-qZSI

Extracting the maximum power from two PV arrays in the same converter is sometimes is a momentous challenge, such as in case of DI-qZSI. For instance, the perturbation of PV_1 has an impact on PV_2; hence, the change in PV_2's power is mixed, and the observation process of PV_2's MPPT is based on both PV arrays perturbations. Based on that, two separate MPPTs for these PV strings may not operate properly. To this regard, an MPPsT algorithm that has the ability to distinguish the impact of both PV arrays perturbations, one on another, has been proposed for the DI-qZSI as shown in Fig. 6.

According to the PV cell $P(v)$ characteristic, the derivative of the PV power with respect to the PV voltage is positive on the left side of the MPP, negative on the right of the MPP, and zero at the MPP,

$$\left.\frac{dP_{\mathrm{PV}}}{dv_{\mathrm{PV}}}\right|_{\mathrm{MPP}} \simeq \left.\frac{\Delta P_{\mathrm{PV}}}{\Delta v_{\mathrm{PV}}}\right|_{\mathrm{MPP}} = 0 \tag{14}$$

Hence, the objective here is to make this derivative equals to zero under any environmental conditions. Among the modifications introduced, is operating two processes during two shifted sampling times as shown in Fig. 6.

At k_B-1 instant, PV_2's voltage is perturbed through the DI-qZSI' modulation index using the following formula

$$M = M \pm \Delta M \tag{15}$$

where, ΔM is the modulation index increment. If it is assumed that, the first perturbation is positive then the operating point would move from A_2 to B_2 (see Fig. 5(b)). This may affect PV_1, where its operating point could move to either B_1^+ or B_1^-. When PV_1's perturbation moment comes (k_A instant), first the voltage and current measurements are taken, which are used to calculate the power in PV_1 and PV_2 as well as the change in PV_2's voltage and power

$$\begin{aligned}\Delta v_{\mathrm{PV2}}(k_{\mathrm{A}}) &= v_{\mathrm{PV2}}(k_{\mathrm{A}}) - v_{\mathrm{PV2}}(k_{\mathrm{B}}-1)\\ \Delta P_{\mathrm{PV2}}(k_{\mathrm{A}}) &= P_{\mathrm{PV2}}(k_{\mathrm{A}}) - P_{\mathrm{PV2}}(k_{\mathrm{B}}-1)\end{aligned} \tag{16}$$

The change in PV_2's voltage and power is stored in the controller and would be used in the next sampling time, i.e., in the moment of the perturbation of PV_2. The change in PV_1's voltage and power, which have been calculated between the previous sampling times k_A-1 and k_B-1

$$\begin{aligned}\Delta v_{\mathrm{PV1}}(k_{\mathrm{B}}-1) &= v_{\mathrm{PV1}}(k_{\mathrm{B}}-1) - v_{\mathrm{PV1}}(k_{\mathrm{A}}-1)\\ \Delta P_{\mathrm{PV1}}(k_{\mathrm{B}}-1) &= P_{\mathrm{PV1}}(k_{\mathrm{B}}-1) - P_{\mathrm{PV1}}(k_{\mathrm{A}}-1)\end{aligned} \tag{17}$$

are used to evaluate the sign of the right tracking direction of PV_1, as shown in Fig. 6, which is then applied through incrementing or decrementing PV_1's voltage reference (v_{PV1}^{ref})

$$v_{\mathrm{PV1}}^{ref} = v_{\mathrm{PV1}}^{ref} \pm \Delta v \tag{18}$$

such as, Δv is the voltage increment. Note that, PV_1's voltage is regulated at this reference by using two cascaded loops, from v_{PV1} to i_{L1} and from i_{L1} to D_{sh}, as shown in Fig. 7.

If it is assumed that, the first action applied to PV_1 is an incremented voltage, then the operating point would move to C_1^- (which is A_1 or close to it) if it was in B_1, and it would move to C_1^+ if it was in B_1^+. PV_1's perturbation would also leave an effect on PV_2, where its operating point may move to either C_2^+ or C_2^- (which is A_2 or close to it). When the observation moment of PV_2 comes (k_B), the measurements are recorded, and the differences in both PV arrays voltages and powers are calculated using (16) and (17). At this stage, the movement of the operating point toward C_2^+ or C_2^- is compared to the one caused by PV_2's perturbation, i.e., the change of power in PV_2 due to the perturbation of PV_2 as well as PV_1, are compared as described by (19).

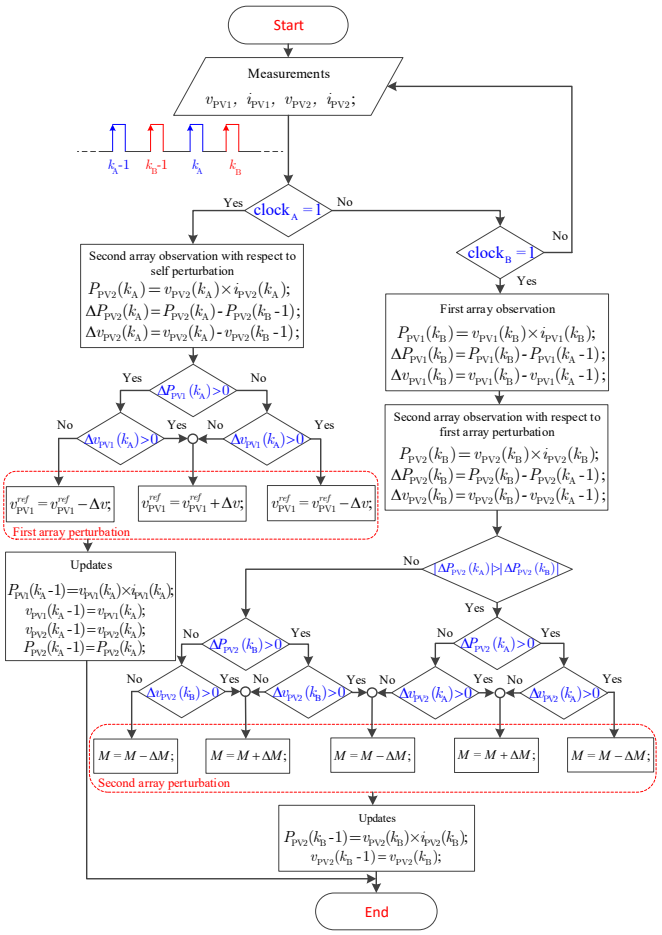

Fig. 6. The proposed MPPsT algorithm for the DI-qZSI.

TABLE II.
COMPARISON OF THE PROPOSED TOPOLOGY WITH ITS COUNTERPARTS

Topologies	Reported in [27]	AAI [28]	Reported in [29]	DI-CCI [30]	DI-qZSI
DC-voltage utilization	v_{PV1} or v_{PV2}	v_{PV1} or v_{PV2}	v_{PV1} and v_{PV2}	$> v_{PV1}$ and v_{PV2}	v_{PV1} and v_{PV2}
Switching frequency	Medium	Medium	High	High	High
Phases	1	1	1	3	3
Capacitors	2	2	4	3	3
Inductors	2	2	2	2	2
Active switches	6	6	8	10	6
Diodes	-	3	4	-	1

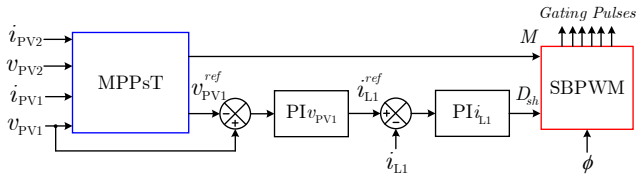

Fig. 7. Control schematic of the DI-qZSI for PV application.

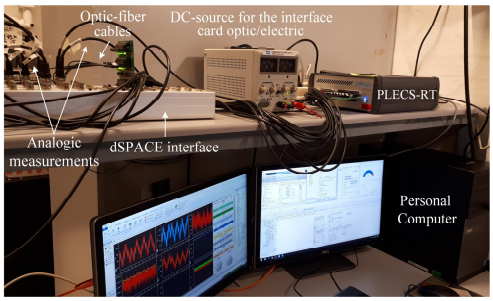

Fig. 8. RT-HIL experimental setup.

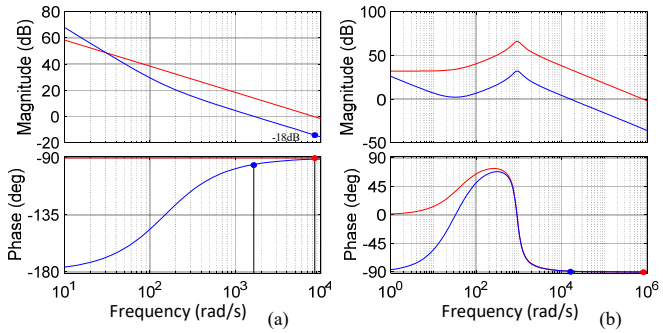

Fig. 9. The frequency response of: (a) $G_{\tilde{i}_{L1}}^{\tilde{v}_{PV1}}$; (b) $G_{\tilde{d}_{sh}}^{\tilde{i}_{L1}}$. The red and blue colors are for the plants with and without controller, respectively.

$$|\Delta P_{PV2}(k_A)| > |\Delta P_{PV2}(k_B)| \tag{19}$$

The term having more weight would be the one used in taking the decision of whether M should be incremented or decremented, as shown in Fig. 6, i.e., if the impact of the self-perturbation of PV_2 ΔM is greater, the decision is taken basedon the change in power and voltage caused by PV_2's perturbation, otherwise, the decision is taken based on the change in power and voltage caused by PV_1's perturbation.

VI. Comparative Analysis

TABLE II. shows a comparison between the proposed topology and some of its well known counterparts namely, the topology reported in [27], Aalborg Inverter (AAI) [28], the topology reported in [29], and the DI central capacitor inverter (DI-CCI) [30] in terms of DC-voltage utilization, switching frequency, phases number, passives count as well as semiconductor devices count. Note that, the output filter elements have been excluded in this table. As it can be seen from this table, the topology reported in [27], AAI, and the topology reported in [29] are single phase ones, where the former two operate with lower DC-voltage utilization. The DI-CCI, as well as the DI-qZSI, are three phase ones with full DC-voltage utilization. Comparing the DI-qZSI to the DI-CCI, it can be seen that the proposal incorporate four less active switches, while only one diode is added.

VII. Hardware-In-the-Loop Experimental Verification

A. Setup specifications

In order to test the effectiveness of the proposal, real-time hardware in the loop (RT-HIL) tests have been performed. The RT-HIL experimental setup used for these tests is shown in Fig. 8, and it comprises of 1) PLECS RT-Box, to which the power hardware circuit of 3.3kW-450V in the first input and 0.4kW-150V in the second input, has been developed in PLECS environment and then, is built and uploaded to. The discretization step size was chosen to be 2μs, considering that the program is executed within 90% of that time. 2) dSPACE1103 controller board for running the control program and generating the gating pulses of 12.5 kHz. 3) Analogic measurement cables for transmitting the measured variables in PLECS RT-Box to the dSPACE. 4) Optic-fiber cables for sending the gating pulses in order to ensure that the electromagnetic interference is not picked up during the transportation process. 5) DC-source for feeding the conditioning board, which was used to convert the digital signals from optic to electric. 6) Personal computer for monitoring and data collection.

The elements of the converter and load are listed in TABLE III. The PV panels were AV-72 model from Abound Solar, whose specification under the standard test conditions (STC) are as the following: $v_{MPP\text{-}STC}$=33.6V, $i_{MPP\text{-}STC}$=2.2A, $v_{OC\text{-}STC}$=47.6V, $i_{SC\text{-}STC}$=2.34A. The array PV_1 was composed of three strings, nine series PV modules in each, in order to reach the desired voltage and current levels, while PV_2 was a three series PV modules. The MPPsT sampling frequency has been set to 20Hz, considering that each PV array is perturbed every 0.1s. The increment Δv has been set to 1V, whereas ΔM was 0.003 to ensure an optimized MPPsT efficiency.

B. Controller parameters design

A compromise between the dynamic performance and the steady state stability has been taken into account in the control parameters design of the DI-qZSI. The frequency response of the transfer functions $G_{\tilde{i}_{L1}}^{\tilde{v}_{PV1}}$ and $G_{\tilde{d}_{sh}}^{\tilde{i}_{L1}}$ are shown in red color in Fig. 9(a), and (b), respectively. Their frequency response under PI controllers compensations are shown in the same figures in blue. The proportional and integral gains of PIv_{PV1} were 0.2 and 30, respectively, whereas those of PIi_{L1} were 0.02 and 0.5, respectively. As it can be seen from Fig. 9(a), the gain of $G_{\tilde{i}_{L1}}^{\tilde{v}_{PV1}}$ after compensation has been set to -18dB at the cross-over frequency of $G_{\tilde{i}_{L1}}^{\tilde{v}_{PV1}}$, which is close enough to

TABLE III.
Converter and Load Elements

Parameter	Value	Parameter	Value
Load inductance, L	8mH	$L_{1,2}$	1mH
Load resistance, R	15Ω	$r_{L1,2}$	0.3Ω
C_{PV1}	120μF	$C_{1,2}$	400μF

-20dB. It can be noted from Fig. 9(a) that, the chosen parameters of PIi_{L1} have been chosen in a way, a faster response without loss of stability is guaranteed. Furthermore, one can see from Fig. 9(a), and (b) that, for stable control loops, the voltage v_{PV1} loop bandwidth has been selected less than tenfold i_{L1} loop bandwidth, where the later itself has been set to be sufficiently lower than the hardware bandwidth (f_s).

C. Tests and results

1) Start-up, considering both PV arrays are under the STC: Fig. 10 shows the obtained results of the proposed idea, where both PVs were subjected to the STC. The extracted powers are shown in Fig. 10(a) and (c). As it can be seen from this figure, both PV arrays are operating at their maximum power. Both M and v_{PV1}^{ref} in this figure are perturbing in three-point pattern, the maximum power point, one point on the left side of the MPP, and one point on the right side of the MPP$_{\{1,2\}}$. It is worth noting that, the qZ-network's inductor currents are operating with minimal ripple, 2.5A each.

For further investigation, a zoom of this test is provided in Fig. 10(az), (bz), (cz), and (dz). One can see from this figure that, PV$_1$'s voltage is completely independent on PV$_2$'s power, as it has reached MPP$_1$ at 0.7s, and continued to perturb in three-point pattern although PV$_2$ was still approaching MPP$_2$. As it can be also observed from this figure, the power of PV$_2$ has been decreased in between two samples of M perturbation due to the perturbation of PV$_1$'s voltage as indicated by the dashed line across Fig. 10(bz), (cz), and (dz). However, the MPPsT did not show any confusion, and M has continued approaching MPP$_2$, and once MPP$_2$ locus has been achieved, M has started to perturb in three-point pattern. The PV harvesting efficiency has been calculated as 99.87% in this test, by using the following formula:

$$\eta = \frac{1}{\left(P_{MPP1}+P_{MPP2}\right)\times T_M}\sum_{i=1}^{n}\left(P_{PV1}^{i}+P_{PV2}^{i}\right)\times\Delta T \quad (20)$$

where T_M, ΔT, and n are, respectively, the total measurement time, the sampling period of the efficiency calculation loop, and the total number of periods.

2) PV$_1$ is shaded: Another test consists of applying an abrupt irradiance decrease in PV$_1$ is shown this paper. The irradiance of PV$_1$ has been decreased by $400\mathrm{W/m^2}$, whereas PV$_2$'s irradiance was under the STC again. The results of this test are shown in Fig. 11. As it can be seen from this figure, as the irradiance decreases, v_{PV1}^{ref} decreases in order to match the new MPP$_1$. One should notice that, the power in PV$_2$ has been also decreased since it is regulated through the total injected current by M. Nevertheless, the proposed MPPsT has decreased M to match back MPP$_2$ locus, without showing any bewilderment, yielding in shorter response time, thus achieving an optimized harvesting efficiency of 99.83%. The voltage seen by the load, which is v_{C1}, is shown in Fig. 11(h). As one can see from this plot, the capacitor C_1 voltage has been affected along with the voltage decrease in both PV$_1$ and PV$_2$ as it is considered to be the sum of these two voltages in average as described by (3).

3) PV$_2$ array is shaded: Another test was done in the other way around. The environmental conditions were at the STC in PV$_1$, whereas PV$_2$'s irradiance was suddenly decreased by $500\mathrm{W/m^2}$. The obtained results when the system was under such conditions are shown in Fig. 12. One can see from Fig. 12(c) and (d) that, the proposed tracker is prompt, as M executing wrong tracking directions. As it can be observed from Fig. 12(a) and (b), when the solar irradiance decreased in

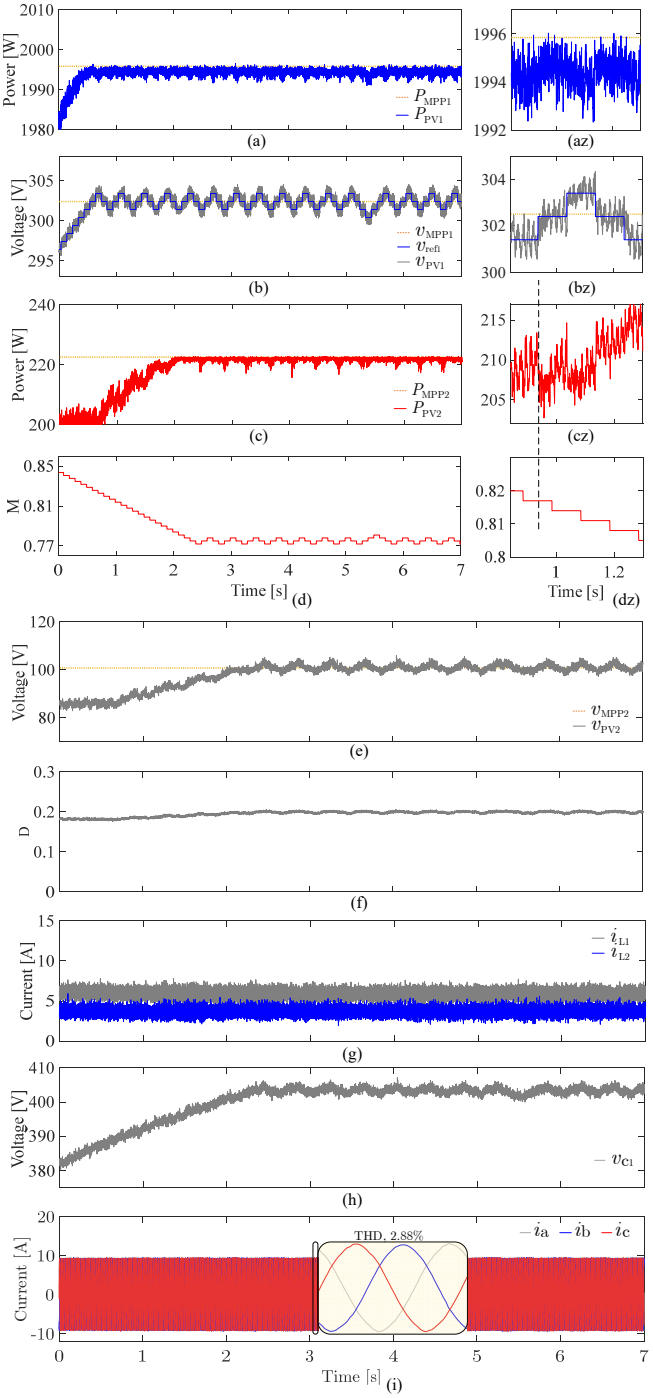

Fig. 10. RT-HIL results of the DI-qZSI operating under the STC The index "z" denotes to zoomed view on the respective figure.

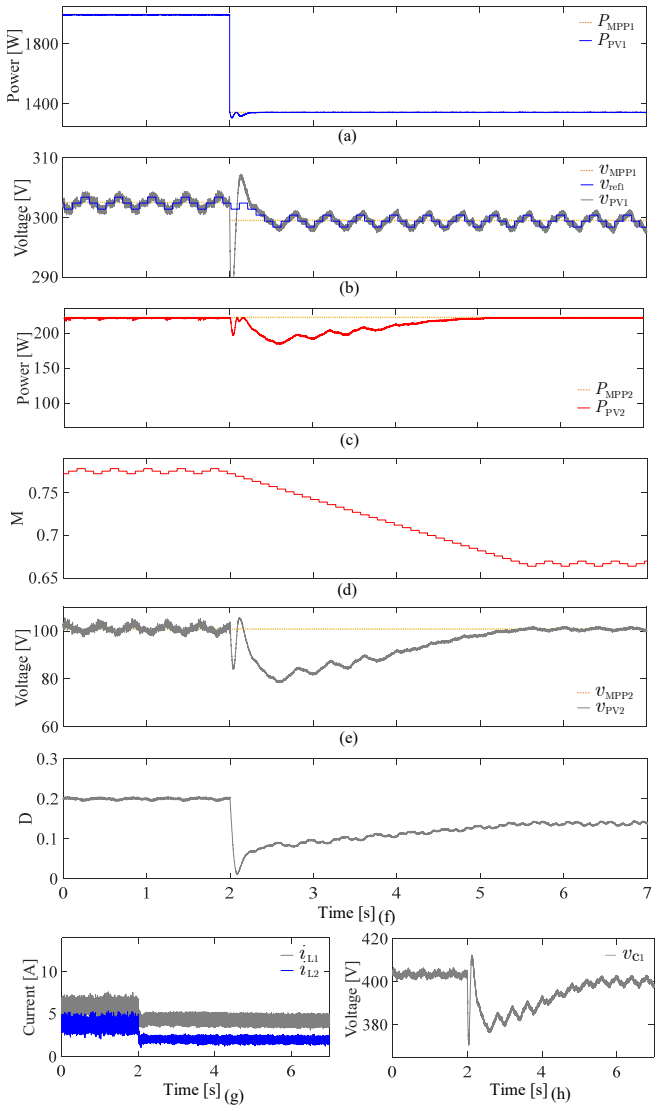

Fig. 11. RT-HIL results of the DI-qZSI, where the irradiance in PV_1 was 600W/m^2, while PV_2 was operating under the STC.

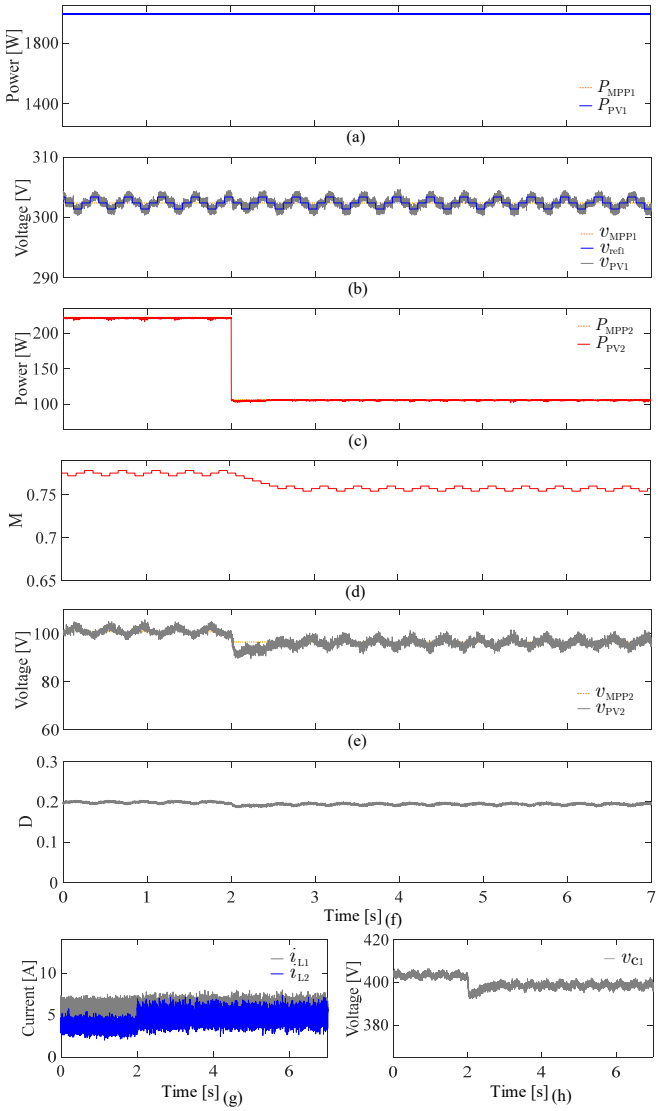

Fig. 12. RT-HIL results of the DI-qZSI, where PV_1 was under the STC, whereas PV_2's irradiance was 500W/m^2.

PV_2, PV_1 was not affected and its reference was provided around v_{MPP1}, registering a PV harvesting efficiency of 99.79%. From Fig. 12(g), it can be seen that the difference between i_{L1} and i_{L2} is minor as i_{PV2} decreased, which is consistent with (6). It can be seen from PV_1 and PV_2 voltages that they suffer from fewer overshoots in this test, which is due to the smaller power harvested by PV_2 caused by the solar irradiance decrease in it.

4) Both PV arrays are shaded: Fig. 13 shows the system behavior when both PV arrays experience a changing solar irradiance. The system starts first operating with both PV arrays under the STC, after 2s, the irradiance in PV_1 decreases suddenly by $400\mathrm{W/m^2}$, and after 7.5s, the solar irradiance decreases in PV_2 by 500W/m^2. As it can be seen from Fig. 13 when the irradiance decreases in PV_1, the MPPsT decreases its voltage reference to match the new MPP locus. M also decreases since the total current injected to the load should be decreased in order to maintain the MPP in PV_2. When the solar irradiance decreases in PV_2, PV_1 was not affected, and the MPPsT kept perturbing PV_1's voltage around v_{MPP1}, yielding in a PV harvesting efficiency of 99.76%.

Based on the previously performed RT-HIL experimental tests, it can be stated that the proposed DI-qZSI is flexible since the arrays are able to operate at different power levels without affecting one another, reaching an optimized efficiency even during partial shading.

5) qZ-Impedance design investigation: Fig. 14 shows the current and voltage ripples in the qZ-network inductors and capacitors, respectively. The tests test-1, test-2, test-3, and test-4 correspond to the previously performed tests, in addition to test-5, in which the added PV array has been removed in order to observe its effect on the current and voltage ripples.

Comparing the ripples in test-1 by those of test-5 it can be stated that the added PV array does not affect the design of the

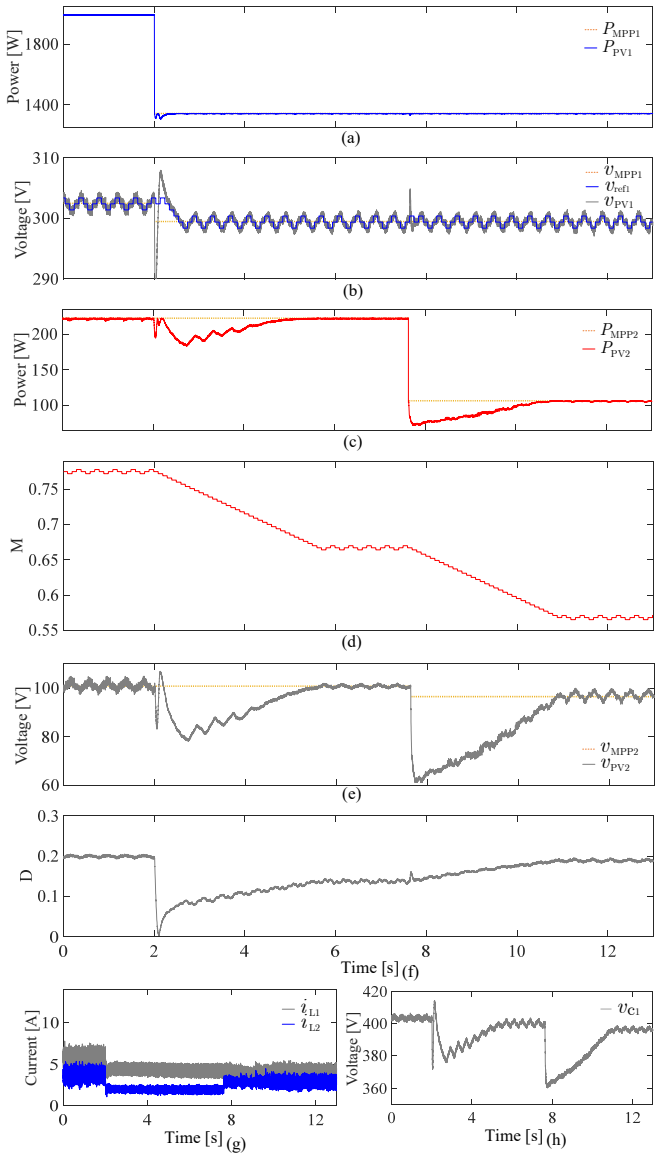

Fig. 13. RT-HIL results of the DI-qZSI, where the solar irradiance changes in both PV arrays.

qZ-network passives, as the differences are minor. The ripple is less in test-2 and -4, but this is due to the total power decrease caused by the solar irradiance change.

D. Conversion Efficiency:

In order to estimate the conversion efficiency of the DI-qZSI and compare it with the conventional qZSI, they have been both thermally modelled in PLECS according to real datasheets. The active switches were insulated gate bipolar transistor (IGBT) type from the model NGTB15N60S1EG, while the qZ-network diode was from ISL9R1560PF2 model. Fig. 15 shows the conduction, the switching, and the inductors L_1 and L_2 stray loss, as well as the resulted conversion efficiencies in both the conventional and DI-qZSI. Note that, in this figure, the loss and efficiencies at each point are calculated considering both PV_1 and PV_2 are subjected to

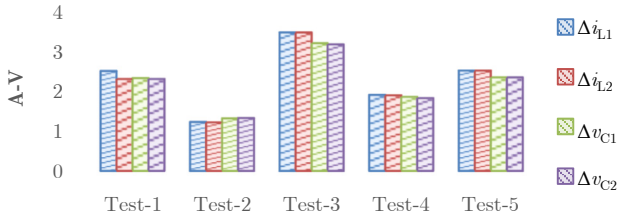

Fig. 14. The current and voltage ripples in the qZ-network passives.

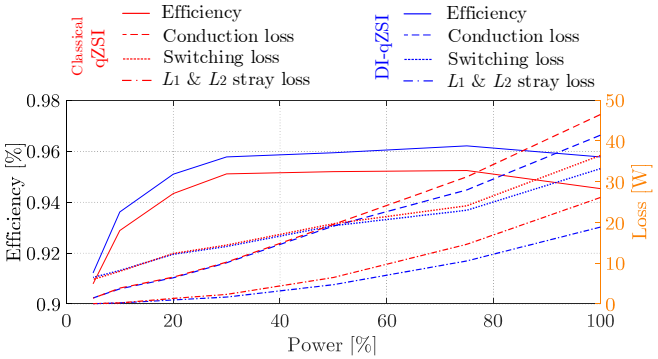

Fig. 15. The conversion efficiency, the conduction, the switching, and the inductors L_1 and L_2 stray loss in both the conventional and DI-qZSI.

similar solar irradiance level. As it can be seen from this figure, the DI-qZSI suffers from less conduction and switching loss compared to the conventional one, which is due to the less current stress on the switches since the inductor L_2 does not conduct all the current of PV_1. Indeed, the current of the later is split and part of it passes through PV_2. The fact that the inductor L_2 conducts less current in the DI-qZSI alleviates the overall loss in the inductors as well, especially under high solar irradiance levels, as shown in Fig. 15. The conventional qZSI registered a maximum conversion efficiency of 95.24%, whereas in the DI-qZSI it reached 96.21%.

VIII. Conclusion

A PV fed DI-qZSI along with its control strategy were the proposal of this paper. A small signal modelling has been presented, showing that the stability of the DI-qZSI with the added PV array is equivalent to that of the classical qZSI. The proposed idea is cost effective, as it does not require installing more elements in the qZSI. Furthermore, it has been demonstrated that the same size as the qZ-network's passive elements in the conventional qZSI can be used here. For optimum use of PV_2, guidelines for its design have been given, where it has been shown that the current in PV_1 should be always greater than that of PV_2 even under partial shading.

The proposal of adding a PV array in parallel to C_2 of the qZ-network comes with the challenge of operating both PV arrays at their MPPs since their powers are shuffled in qZ-network. Thus, an MPPsT algorithm, which has the ability to discriminate the impact of both PV arrays perturbations, one on another, has been proposed in this work. The proposed concept has been experimentally implemented, where the PV

arrays have been tested under different weather conditions. By setting the optimal MPPsT parameters, the proposed algorithm still does not show any confusion issue between the two controlled PV powers under any of the tested conditions.

It has to be acknowledged that, the developed MPPsT controller has been designed considering that both PV_1 and PV_2 have one MPP point, each. The MPPsT is envisaged to be extended in future work for partial shading cases, where each of PV_1 and PV_2 has several MPP points.

IX. References

[1] Y. Zhou, L. Liu, and H. Li, "A High-Performance Photovoltaic Module-Integrated Converter (MIC) Based on Cascaded Quasi-Z-Source Inverters (qZSI) Using eGaN FETs," *IEEE Trans. Power Electron.*, vol. 28, no. 6, pp. 2727-2738, June 2013.

[2] N. Kumar, I. Hussain, B. Singh and B. K. Panigrahi, "Implementation of Multilayer Fifth-Order Generalized Integrator-Based Adaptive Control for Grid-Tied Solar PV Energy Conversion System," *IEEE Trans. Ind. Info.*, vol. 14, no. 7, pp. 2857-2868, July 2018.

[3] F. Lin, K. Lu, T. Ke, B. Yang and Y. Chang, "Reactive Power Control of Three-Phase Grid-Connected PV System During Grid Faults Using Takagi–Sugeno–Kang Probabilistic Fuzzy Neural Network Control," *IEEE Trans. Ind. Electron.*, vol. 62, no. 9, pp. 5516-5528, Sept. 2015.

[4] Z. Zhou, X. Zhang, P. Xu, and W. X. Shen, "Single-phase uninterruptible power supply based on Z-source inverter," *IEEE Trans. Ind. Electron*., vol. 55, no. 8, pp. 2997–3004, Aug. 2008.

[5] Y. Liu *et al*., "Control system design of battery-assisted quasi-z-source inverter for grid-tie photovoltaic power generation," *IEEE Trans. Sustain. Energy*, vol. 4, no. 4, pp. 994–1001, 2013.

[6] F. Z. Peng, "Z-source inverter,"*IEEE Trans. Ind. Appl.*, vol. 39, no. 2, pp. 504-510, Mar/Apr 2003.

[7] J. Liu *et al*., "Dynamic Modeling and Analysis of Z Source Converter—Derivation of AC Small Signal Model and Design-Oriented Analysis," *IEEE Trans. Power Electron.*, vol. 22, no. 5, pp. 1786-1796, Sept. 2007.

[8] F. Bradaschia *et al.*, "Modulation for Three-Phase Transformerless Z-Source Inverter to Reduce Leakage Currents in Photovoltaic Systems," *IEEE Trans. Ind. Electron*., vol. 58, no. 12, pp. 5385-5395, Dec. 2011.

[9] Y. Li *et al*., "Modeling and Control of Quasi-Z-Source Inverter for Distributed Generation Applications," *IEEE Trans. Ind. Electron.*, vol. 60, no. 4, pp. 1532-1541, April 2013.

[10] M. Shen *et al*., "Constant boost control of the Z-source inverter to minimize current ripple and voltage stress," *IEEE Trans. Ind. Appl*., vol. 42, no. 3, pp. 770–778, May/Jun. 2006.

[11] F. Z. Peng *et al*., "Maximum boost control of the Z-source inverter," *IEEE Trans. Power Electron*., vol. 20, no. 4, pp. 833–838, July. 2005.

[12] Y. Li, J. Anderson, F. Z. Peng and D. Liu, "Quasi-Z-Source Inverter for Photovoltaic Power Generation Systems," 24th *Ann. IEEE Appl. Power Electron. Conf. Expo.*, Washington, DC, 2009, pp. 918-924.

[13] B. Ge *et al*.,"Current Ripple Damping Control to Minimize Impedance Network for Single-Phase Quasi-Z Source Inverter System," *IEEE Trans. Ind. Info.*, vol. 12, no. 3, pp. 1043-1054, June 2016.

[14] H. Abu-Rub *et al*., "Quasi-Z-Source Inverter-Based Photovoltaic Generation System With Maximum Power Tracking Control Using ANFIS," *IEEE Trans. Sust. Energy*, vol. 4, no. 1, pp. 11-20, Jan. 2013.

[15] D. Vinnikov and I. Roasto, "Quasi-Z-Source-Based Isolated DC/DC Converters for Distributed Power Generation," *IEEE Trans. Ind. Electron.*, vol. 58, no. 1, pp. 192-201, Jan. 2011.

[16] A. Chub *et al*., "Multiphase Quasi-Z-Source DC–DC Converters for Residential Distributed Generation Systems," *IEEE Trans. Ind. Electron*., vol. 65, no. 10, pp. 8361-8371, Oct. 2018.

[17] Y. Liu, H. Abu-Rub and B. Ge, "Front-End Isolated Quasi-Z-Source DC–DC Converter Modules in Series for High-Power Photovoltaic Systems—Part I: Configuration, Operation, and Evaluation," *IEEE Trans. Ind. Electron.*, vol. 64, no. 1, pp. 347-358, Jan. 2017.

[18] F. Guo, L. Fu, C. Lin, C. Li, W. Choi and J. Wang, "Development of an 85-kW Bidirectional Quasi-Z-Source Inverter With DC-Link Feed-Forward Compensation for Electric Vehicle Applications," *IEEE Trans. Power Electron*., vol. 28, no. 12, pp. 5477-5488, Dec. 2013.

[19] S. Hu, Z. Liang, D. Fan and X. He, "Hybrid Ultracapacitor–Battery Energy Storage System Based on Quasi-Z-source Topology and Enhanced Frequency Dividing Coordinated Control for EV," *IEEE Trans. Power Electron*., vol. 31, no. 11, pp. 7598-7610, Nov. 2016.

[20] D. Sun *et al*., "Modeling, Impedance Design, and Efficiency Analysis of Quasi-ZSource Module in Cascaded Multilevel Photovoltaic Power System," *IEEE Trans. Ind. Electron*., vol. 61, no. 11, pp. 6108-6117, Nov. 2014.

[21] Y. Liu *et al*., "An Effective Control Method for Quasi-Z-Source Cascade Multilevel Inverter-Based Grid-Tie Single-Phase Photovoltaic Power System," *IEEE Trans. Ind. Info.*, vol. 10, no. 1, pp. 399-407, Feb. 2014.

[22] O. Ellabban, H. Abu-Rub and B. Ge, "A Quasi-Z-Source Direct Matrix Converter Feeding a Vector Controlled Induction Motor Drive," *IEEE J. Emerg. Sel. Top. Power Electron.*, vol. 3, no. 2, pp. 339-348, June 2015.

[23] J. Khajesalehi *et al*., "High-performance hybrid photovoltaic -battery system based on quasi-Z-source inverter: application in microgrids," *IET Gener. Transm. Distrib.*, vol. 9, no. 10, pp. 895–902, 2015.

[24] D. Sun *et al*., "An Energy Stored Quasi-Z-Source Cascade Multilevel Inverter-Based Photovoltaic Power Generation System," *IEEE Trans. Ind. Electron.*, vol. 62, no. 9, pp. 5458-5467, Sept. 2015.

[25] W. Liang *et al*., "Double-Line-Frequency Ripple Model, Analysis, and Impedance Design for Energy-Stored Single-Phase Quasi-Z-Source Photovoltaic System," *IEEE Trans. Ind. Electron.*, vol. 65, no. 4, pp. 3198-3209, April 2018.

[26] B. Peng, K. Ho and Y. Liu, "A Novel and Fast MPPT Method Suitable for Both Fast Changing and Partially Shaded Conditions," *IEEE Trans. Ind. Electron*. vol. 65, no. 4, pp. 3240-3251, April 2018.

[27] D. Debnath and K. Chatterjee, "Maximising power yield in a transformerless single phase grid connected inverter servicing two separate photovoltaic panels," *IET Renewable Power Gener*., vol. 10, no. 8, pp. 1087–1095, 2016.

[28] W. Wu, J. Ji, and F. Blaabjerg, "Aalborg inverter a new type of buck in buck, boost in boost grid-tied inverter," *IEEE Trans. Power Electron.*,vol. 30, no. 9, pp. 4784–4793, Sep. 2015.

[29] S. Dutta and K. Chatterjee, "A Buck and Boost Based Grid Connected PV Inverter Maximizing Power Yield From Two PV Arrays in Mismatched Environmental Conditions," *IEEE Trans. Ind. Electron.*, vol. 65, no. 7, pp. 5561-5571, July 2018.

[30] M. Chen, F. Gao and C. Jia, "Operation of dual-input central capacitor photovoltaic inverter under unbalanced grid voltage condition," *IEEE Energy Conv. Congr. Expo.*, Milwaukee, WI, 2016, pp. 1-7.

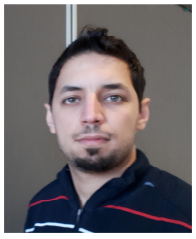

Abderezak Lashab (S'13) received the bachelor's and master's degrees in electrical engineering in 2010 and 2012, respectively, from Universié des Frères Mentouri Constantine, Constantine, Algeria. During the year 2013, he served as an engineer in High Tech Systems (HTS).

He is currently working toward the Ph.D. degree with the Department of Energy technology, Aalborg University, Denmark. His current research interests include topologies, control, modeling, and diagnostics of power electronics for renewable energy applications.

Dezso Sera (S'05–M'08–SM'15) received the B.Sc. and M.Sc. degrees in electrical engineering from the Technical University of Cluj, Cluj-Napoca, Romania, in 2001 and 2002, respectively, the M.Sc. degree in power electronics and the Ph.D. degree in PV systems from the Department of Energy Technology, Aalborg University, Aalborg, Denmark, where he is currently an Associate Professor. Since 2009, he has been a Leader of the Photovoltaic Systems Research Program (www.pv-systems.et.aau.dk) at the same department.

His research interests include modeling, characterization, diagnostics and maximum power point tracking (MPPT) of PV arrays, as well as power electronics, and grid integration for PV systems.

João Martins (S'17) received the B.Sc. degree in electrical engineering from the Polytechnic Institute of Lisbon, Lisbon, Portugal in 2014. He received the M.Sc. degree in power electronics and drives from the Department of Energy Technology, Aalborg University, Aalborg, Denmark, in 2017, during which he spent 6 months at ABB corporate research, Vasteras, Sweden. He is currently a research assistant at Department of Energy Technology, Aalborg University.

His research interests include power electronics topologies and control for renewable energy applications.

Josep M. Guerrero (S'01–M'04–SM'08–F'15) received the B.S. degree in telecommunications engineering, the M.S. degree in electronics engineering, and the Ph.D. degree in power electronics from the Technical University of Catalonia, Barcelona, Spain, in 1997, 2000, and 2003, respectively. Since 2011, he has been a Full Professor with the Department of Energy Technology, Aalborg University, Aalborg, Denmark, where he is responsible for the Microgrid Research Program. In 2012, he was a Guest Professor with the Chinese Academy of Science and the Nanjing University of Aeronautics and Astronautics; and in 2014, he was the Chair Professor with Shandong University.

His research interests include different microgrid aspects, including power electronics, distributed energy-storage systems, hierarchical and cooperative control, energy management systems, and optimization of microgrids and islanded minigrids.

Dr. Guerrero was awarded by Thomson Reuters as an ISI Highly Cited Researcher